Title
Resonant ultrasound spectroscopic techniques for measurement of the elastic moduli of solids

Journal
Physica B Condensed Matter, 183(1-2)

ISSN
0921-4526

Authors
Migliori, A
Sarrao, JL
Visscher, William M
et al.

Publication Date
1993

DOI
10.1016/0921-4526(93)90048-b

Physica B 183 (1993) 1–24
North-Holland

PHYSICA B

Resonant ultrasound spectroscopic techniques for measurement of the elastic moduli of solids

A. Migliori, J.L. Sarrao, William M. Visscher, T.M. Bell, Ming Lei, Z. Fisk[1] and R.G. Leisure[2]

Los Alamos National Laboratory, Los Alamos, NM, USA

Received 20 October 1992

The mechanical resonant response of a solid depends on its shape, density, elastic moduli and dissipation. We describe here instrumentation and computational methods for acquiring and analyzing the resonant ultrasound spectrum of very small (0.001 cm^3) samples as a function of temperature, and provide examples to demonstrate the power of the technique. The information acquired is in some cases comparable to that obtained from other more conventional ultrasonic measurement techniques, but one unique feature of resonant ultrasound spectroscopy (RUS) is that all moduli are determined simultaneously to very high accuracy. Thus in circumstances where high relative or absolute accuracy is required for very small crystalline or other anisotropic samples RUS can provide unique information. RUS is also sensitive to the fundamental symmetry of the object under test so that certain symmetry breaking effects are uniquely observable, and because transducers require neither couplant nor a flat surface, broken fragments of a material can be quickly screened for phase transitions and other temperature-dependent responses.

1. Introduction

Large single crystals are always highly prized, in part because of their appearance, but also because usually they are the result of considerable effort on the part of the grower. Such effort is justified because the usual implementation of many measurement techniques, for various complex and often mundane reasons, requires samples with dimensions in the centimeter range. Ultrasound measurements, traditionally of great importance because of their connection to thermodynamics, transport properties and microstructural effects, are typically subject to this size constraint. When only small samples are available, it is possible to perform pulse-echo ultrasound measurements at GHz frequencies [1] or to use the vibrating reed and related methods [2], but the cost to the scientist is either instrument complexity or loss of information. There are, of course, other nonacoustic techniques for obtaining sound velocity and attenuation data such as Brillouin scattering [3], inelastic neutron scattering [4], X-ray based methods [5] and others. Each of these nonacoustic techniques has advantages and disadvantages. Among the disadvantages common to all of them is the lack of high precision. Only the acoustic techniques can achieve 10^{-6} or better reproducibility. Because the speed of sound may vary only a percent or less at a phase transition [6] or a few percent from 300 K to 4 K, this lack of precision can be a serious failing. On the other hand, neutron scattering can provide the entire dispersion curve from Brillouin-zone center to edge, but with worse than percent accuracy, Brillouin scattering can obtain data at frequencies in the tens of GHz range with 1% accuracy on very small samples but suffers at cryogenic temperatures or with

Correspondence to: A. Migliori, Los Alamos National Laboratory, MSK 764 Los Alamos, NM 87545, USA.
[1] Also at Department of Physics and Institute for Pure and Applied Physical Sciences, University of California, San Diego, La Jolla, CA 92093, USA.
[2] Permanent address: Department of Physics, Colorado State University, Fort Collins, CO 80523, USA.

opaque samples, and X-ray techniques achieve moderate accuracy on very small samples. Thus each of these techniques retains an important place in elasticity studies (or it would not be used, of course).

Of the acoustic techniques, such methods as the vibrating reed and torsion pendulum can measure only some of the elastic moduli, while pulse-echo ultrasound and most of the nonacoustic techniques can measure all of them. This is not a particularly important constraint for isotropic materials such as glasses, polycrystalline metals and ceramics. However, for single crystals, textured alloys and the like, the value of ultrasound measurements is often critically dependent on measurement of all moduli with both precision and accuracy.

This requirement for accuracy and precision is exemplified by ultrasonic studies of the physics surrounding second-order phase transitions. At such transitions, there are no microscopic discontinuities in the material. No atoms suddenly change position, magnetism and ferroelectricity do not suddenly appear, and electrical conductivity in a superconductor becomes infinite only for infinitesimal currents carried at zero magnetic field. However, several thermodynamic second derivatives do exhibit discontinuities. For a liquid, with only one elastic modulus, it is simple to write down the important relations, using pressure (P), volume (V) and temperature (T) instead of stress σ_{ij}, strain ε_{ij} and T. They are

$$\partial^2 \Delta G/\partial P^2 = \partial \Delta V/\partial P = -1/B\,, \tag{1}$$

$$\partial^2 \Delta G/\partial T^2 = -\partial \Delta S/\partial T = -C_p/T\,, \tag{2}$$

$$\partial^2 \Delta G/\partial P\,\partial T = \partial \Delta V/\partial T = \alpha\,, \tag{3}$$

where ΔG is the Gibb's free energy difference per unit volume across the phase boundary and is continuous, ΔV is the fractional volume discontinuity across the phase boundary, equal to zero, ΔS the entropy discontinuity, also zero, C_p is the specific heat, α is the volume thermal expansion coefficient and B the bulk modulus. Each of the quantities C_p, α and B can exhibit discontinuities at T_s, the second-order phase transition temperature at which the high-temperature (usually the so-called symmetric) phase transforms to the low-temperature (usually the unsymmetric) phase.

Discontinuities are of great importance to the experimentalist because they are often the most unambiguous of measured quantities. Moreover, in general C_p is a scalar, α a vector and, if we were to write eq. (1) for stress and strain rather than pressure and volume, we would find that the right side of eq. (1) would be a tensor. That the modulus is a tensor and is discontinuous at a second-order phase transition is a key motivating factor for the development of RUS. To see why, consider a simple soft-mode structural phase transition such as occurs in La_2CuO_4. This transition, described in more detail below, arises from a zone-edge double-well [7] potential V for one phonon branch. As the material in its tetragonal phase is cooled, the thermal excitation level drops through the point where the double well becomes important. The free energy G exhibits a single-well behavior from thermal smearing at high temperature and a double-well behavior cold. At the temperature T_s where the behavior just switches over, the phonon's frequency decreases to zero resulting in a static displacement. This static displacement increases from zero as the material is cooled further, doubling the unit cell to an orthorhombic structure. What is of most interest here is that the zone-edge static displacement, coupled with group theoretical considerations including phonon and crystal symmetry, Ginsburg–Landau theory [8] and fluctuation theory [9], forces very specific predictions about which moduli exhibit discontinuities and how big, and the temperature dependence of the moduli as T_s is approached from either direction. Such an analysis can be made for any second-order phase transition, and, if the full response of the modulus tensor is available, one can work backwards to extract much of the physics driving the transition. Without a discontinuous tensor to work from, such an analysis would be more subject to interpretational errors.

RUS can determine the full elastic tensor in a single measurement with unprecedented absolute

and relative accuracy from cryogenic to very high temperatures. The basic principle behind this simple, inexpensive bench-top measurement technique is that the mechanical resonances of a solid depend on its shape and moduli in a way sufficiently complex such that a measurement of the resonant frequencies of a carefully made sample can be used to determine the full elastic tensor. To illustrate this we show in table 1 the results of such a measurement on a Si_3N_4 ball bearing. These data represent our current state-of-the-art for accuracy, primarily because this object, a nominal 5/16 inch diameter sphere, is spherical to a few parts per million and is made from a carefully controlled ceramic with very isotropic properties. Thus only two moduli, the density and the diameter are required to fully characterize its resonances. As can be seen from the columns labelled f_m and f_r, agreement between experiment and computation is of order 0.01% after a best fit to the moduli (in this case, we use the shear modulus μ and Poisson's ratio σ as the independent parameters) is found. Density and diameter are measured independently. For a larger 1/2 inch nominal-diameter sphere of the same material, we obtain 0.004% agreement, primarily because the larger object is less perturbed by air and transducer contact and because its temperature cannot change as quickly.

2. Measurement techniques

Current practices in the design of the hardware, data analysis and sample preparation systems required to make and interpret RUS measurements have not been described in detail anywhere. Because of the novelty of the technique, and because of its utility, it is important to understand the measurement system in order to appreciate the data produced by it. Because an example is often the best focus, a state-of-the-art apparatus for making low-temperature RUS measurements on rectangular parallelepiped (RP), spherical and cylindrical samples with smallest dimension of about 0.05 cm, from 20 K to 400 K, will be described schematically. Using data on $SrTiO_3$, La_2CuO_4 and $La_{2-x}Sr_xCuO_4$ single crystals, we will illustrate what can be learned with RUS including certain effects relating to crystal symmetries not accessible by any other measurement method.

2.1. Data analysis

The key to the successful application of RUS is the ability to compute mechanical resonances from a body's shape, density and moduli. For solids, such as a sphere or RP, having a shape sufficiently simple to enable description by a few

Table 1
Resonant ultrasound measurement of a 0.63500 cm diameter Si_3N_4 ceramic sphere with a density of 3.2325 g/cm^3. f_m are measured frequencies, f_r are fitted, n is the mode number. k is our designator (to be discussed below) for the symmetry of the mode and i is in essence the harmonic number of each symmetry type. Multiple entries indicate the mode degeneracy. The fit for $\mu = 1.2374 \times 10^{12}$ dyne/cm^2 and $\sigma = 0.2703$ has a χ^2 (%) = 0.0124. This is sufficient to determine μ to about 0.01% and σ to about 0.05%. There are no corrections so these values are absolute.

n	f_r (MHz)	f_m (MHz)	% error	(k, i)
1	0.775706	0.775707	−0.000138	(6, 1), (1, 1), (4, 1), (4, 2), (7, 1)
6	0.819567	0.819983	−0.050778	(5, 1), (3, 1), (5, 2), (8, 1), (2, 1)
11	1.075664	1.075399	0.024614	(1, 2), (7, 2), (6, 2)
14	1.198616	1.198505	0.009239	(5, 3), (2, 2), (3, 2), (8, 2), (3, 3), (8, 3), (2, 3)
21	1.217375	1.217850	−0.039042	(1, 3), (6, 3), (7, 3), (1, 4), (6, 4), (7, 4), (4, 3)
28	1.440760	1.440750	0.000712	(5, 4)
29	1.527080	1.526474	0.039695	(5, 5), (8, 4), (3, 4), (5, 6), (2, 4)
34	1.558358	1.558848	−0.031448	(5, 7), (5, 8), (5, 9), (3, 5), (8, 5), (2, 5), (3, 6), (8, 6), (2, 6)
43	1.580067	1.579871	0.012426	(6, 5), (7, 5), (7, 6), (1, 5), (4, 4), (1, 6), (6, 6), (4, 5), (4, 6)

mathematical functions, an approach based on work by Holland [10], Demarest [11], Anderson et al. [12] and Ohno [13] is used. This procedure does not use finite-element methods but instead seeks stationary points of the Lagrangian for a solid with free surfaces [14], and with a nondissipative symmetric elastic tensor with no far-field effects such as those associated with ferromagnets or ferroelectrics. Far-field systems [15] and the dissipative problem [16] have been analyzed successfully, but will not be discussed here. Once the mechanical resonances are computed (the direct problem), carefully constructed fitting procedures can be used to work backwards to find moduli from resonant frequencies (the inverse problem).

The procedure for solving the direct problem for an arbitrarily shaped elastic solid with volume V, elastic tensor c_{ijkl}, density ρ, and with a free surface S begins with the Lagrangian

$$L = \int_V (\mathrm{KE} - \mathrm{PE})\, \mathrm{d}V \tag{4}$$

where the kinetic energy, KE, is given by

$$\mathrm{KE} = \tfrac{1}{2}\rho\omega^2 u_i^2 , \tag{5}$$

and the potential energy, PE, by

$$\mathrm{PE} = \tfrac{1}{2} c_{ijkl} u_{i,j} u_{k,l} . \tag{6}$$

Here u_i is the ith component of the displacement vector, the usual summation convention applies, indices following a comma denote differentiation with respect to that coordinate and the time dependence of the displacements is assumed to be $\mathrm{e}^{\mathrm{i}\omega t}$ where ω is the angular frequency and t is time.

Following Hamilton, we allow u_i to vary arbitrarily in the volume V and on the surface S ($u_i \rightarrow u_i + \delta u_i$) and calculate the variation δL in L. The result is

$$\delta L = \int_V (\text{left side of eq. (8)})_i \delta u_i \, \mathrm{d}V + \int_S (\text{left side of eq. (9)})_i \delta u_i \, \mathrm{d}S \tag{7}$$

plus higher-order terms in δu_i. The elastic wave equation is

$$\rho\omega^2 u_i + c_{ijkl} u_{k,lj} = 0 , \tag{8}$$

and the vanishing of the ith component of the surface traction vector is expressed by

$$n_j c_{ijkl} u_{k,l} = 0 \tag{9}$$

where $\{n_i\}$ is the unit outer normal to S.

Because of the arbitrariness of δu_i in V and on S, the u_i's which correspond to stationary points of L (i.e. $\delta L = 0$) must satisfy eq. (8) in V and eq. (9) on S. There are no such u_i's, of course, unless ω^2 is one of a discrete set of eigenvalues, the normal mode frequencies of free vibration of the system. This simple result makes possible the following powerful procedure for obtaining the free vibrations of an object.

Following the Rayleigh–Ritz prescription, we expand the displacement vector in a complete set of functions $\{\Phi_\lambda\}$,

$$u_i = a_{\lambda i} \Phi_\lambda , \tag{10}$$

and choose as our basis functions powers of cartesian coordinates:

$$\Phi_\lambda = x^l y^m z^n , \tag{11}$$

where $\lambda = (l, m, n)$ is the function label, a set of three nonnegative integers. After substituting eq. (10) into eq. (4), we obtain ($\boldsymbol{a}$ becomes a column vector)

$$L = \tfrac{1}{2}\omega^2 \boldsymbol{a}^{\mathrm{T}} \boldsymbol{E} \boldsymbol{a} - \tfrac{1}{2} \boldsymbol{a}^{\mathrm{T}} \boldsymbol{\Gamma} \boldsymbol{a} \tag{12}$$

where $\boldsymbol{E}$ and $\boldsymbol{\Gamma}$ are matrices whose order R is determined by the truncation condition

$$l + m + n \leqslant N , \tag{13}$$

with $R = 3(N+1)(N+2)(N+3)/6$. We have found that $N = 10$ gives a good compromise between computational accuracy, computing time and typical sample preparation errors consistent with data spanning the first 50 or so modes.

The matrix $\boldsymbol{E}$ has elements

$$E_{\lambda i\lambda' i'} = \delta_{ii'} \int_V \Phi_\lambda \rho \Phi_{\lambda'} \, \mathrm{d}V \, . \tag{14}$$

If we had chosen Φ_λ to be an orthonormal set with respect to the density ρ (for example, normalized Legendre polynomials [13]), $\boldsymbol{E}$ would have been the unit matrix, simplifying subsequent manipulations. Our choice of Φ_λ, although extracting a moderate computational penalty, is more easily applied to complex shapes than an orthonormal set.

The matrix $\boldsymbol{\Gamma}$ has elements

$$\Gamma_{\lambda i\lambda' i'} = c_{iji'j'} \int_V \Phi_{\lambda,j} \Phi_{\lambda',j'} \, \mathrm{d}V \, . \tag{15}$$

The volume integrals which appear here are quite tractable for many shapes if the choice (11) is made.

The expression (12) for the Lagrangian is stationary if the displacements u_i are solutions of the free-vibration problem. These solutions may be obtained by setting the derivatives of eq. (12) with respect to each of the R amplitudes $a_{i\lambda}$ equal to zero. This yields the following eigenvalue equation:

$$\omega^2 \boldsymbol{E}\boldsymbol{a} = \boldsymbol{\Gamma}\boldsymbol{a} \, . \tag{16}$$

The matrix $\boldsymbol{E}$ is symmetric and positive definite and $\boldsymbol{\Gamma}$ is symmetric, so a standard eigenvalue–eigenvector subroutine package (RSG in EISPACK-[17]) can be used to solve (16).

For our choice of Φ_λ the matrix elements of $\boldsymbol{E}$ and $\boldsymbol{\Gamma}$ are all of the form

$$f(p, q, r) = \int_V x^p y^q z^r \, \mathrm{d}V \, , \tag{17}$$

where p, q and r are nonnegative integers. This integral can be evaluated analytically for a variety of shapes [14]. For the RP with sides $2d_1$, $2d_2$, $2d_3$, it is

$$f(p, q, r) = \frac{8 d_1^{p+1} d_2^{q+1} d_3^{r+1}}{(p+1)(q+1)(r+1)} \, . \tag{18}$$

To solve the inverse problem, the derivatives of the eigenfrequencies $f = \omega/2\pi$ (where ω^2 is an eigenvalue of eq. (16)) with respect to parameters of the sample are required. These can be obtained easily in the following way. First, differentiate eq. (16) with respect to one of the sample parameters p (an elastic constant, dimension or angle specifying the orientation of the crystallographic axes with respect to the parallelepipedal axes) to obtain

$$\begin{aligned} &\partial\omega^2/\partial p \, \boldsymbol{E}\boldsymbol{a} + \omega^2 \boldsymbol{E} \, \partial\boldsymbol{a}/\partial p + a\omega^2 \, \partial\boldsymbol{E}/\partial p \, \boldsymbol{a} \\ &\quad = \partial\boldsymbol{\Gamma}/\partial p \, \boldsymbol{a} + \boldsymbol{\Gamma} \, \partial\boldsymbol{a}/\partial p \, . \end{aligned} \tag{19}$$

Then multiply this from the left with $\boldsymbol{a}^{\mathrm{T}}$ and compare with the transpose of eq. (16) to get

$$\partial\omega^2/\partial p = (\boldsymbol{a}^{\mathrm{T}}[\partial\boldsymbol{\Gamma}/\partial p - \omega^2 \, \partial\boldsymbol{E}/\partial p]\boldsymbol{a}) \, . \tag{20}$$

Because we have already computed the eigenvectors $\boldsymbol{a}$ and the volume integrals occurring in $\partial\boldsymbol{\Gamma}/\partial p$ and $\partial\boldsymbol{E}/\partial p$ are trivial, the computation of the derivatives represents only a minor increase in computational time.

We can speed up the calculation immensely by exploiting the symmetries $x \to -x$, $y \to -y$, $z \to -z$ that occur if the crystal is of orthorhombic or higher symmetry and the crystallographic axes are aligned with those of the sample. Then by inspection of the PE in eq. (6) we see that if u_x is characterized by a parity triplet $(-\xi, \mu, \nu)$ where

$$-\xi = (-1)^l, \quad \mu = (-1)^m, \quad \nu = (-1)^n \, ,$$

the matrix $\boldsymbol{\Gamma}$ only connects this u_x with u_y and u_z having the following parities:

$$\begin{aligned} &u_x : (-\xi, \mu, \nu) \, , \\ &u_y : (\xi, -\mu, \nu) \, , \\ &u_z : (\xi, \mu, -\nu) \, . \end{aligned} \tag{21}$$

Thus the matrix $\boldsymbol{\Gamma}$ degenerates into a block-diagonal matrix with eight blocks, each characterized by one parity triplet, say the parity of u_x. We label this parity as follows:

$$k = \begin{matrix} 1 & 2 & 3 & 4 & 5 & 6 & 7 & 8 \end{matrix}$$

$$\begin{pmatrix} \xi \\ \mu \\ \nu \end{pmatrix} = \begin{pmatrix} + \\ + \\ + \end{pmatrix}\begin{pmatrix} + \\ + \\ - \end{pmatrix}\begin{pmatrix} + \\ - \\ + \end{pmatrix}\begin{pmatrix} + \\ - \\ - \end{pmatrix}\begin{pmatrix} - \\ + \\ + \end{pmatrix}\begin{pmatrix} - \\ + \\ - \end{pmatrix}\begin{pmatrix} - \\ - \\ + \end{pmatrix}\begin{pmatrix} - \\ - \\ - \end{pmatrix}. \tag{22}$$

The modes for each k-value (22) are uncoupled, so that the maximum order for which we need to solve the eigenvalue problem (16) and the total computational time are much reduced even though we now have 8 eigenvalue problems to solve.

Each of the 8 k-values represents a different symmetry for the displacement of the material in the object. For example a uniform translation in the x-direction will have u_x with $(l, m, n) = (0, 0, 0)$ or $k = 1$. A translation in the y-direction has $k = 7$, and a translation in the z-direction $k = 6$. Similarly, a rotation about the z-axis will have $k = 3$, one about the y-axis has $k = 2$, and one about the x-axis $k = 4$. These six special eigenvectors all have an eigenvalue of zero. One other special case occurs for $k = 5$ which has div $\boldsymbol{u} \neq 0$ after averaging over V, so it is the only k-value for which the volume oscillates.

This very fast and accurate solution to the direct problem is the key tool for solution of the inverse problem. However, the inverse problem is not at all straightforward. First note that there is no unique solution to the inverse problem because all the frequencies scale inversely with the linear dimensions of the sample and with the square root of the elastic constants. This simple scaling problem is easily dealt with, but for real data on imperfect objects, other uniqueness problems arise that are difficult to circumvent. The best procedure we have found is to begin with a 'figure of merit':

$$F = \sum_i w_i (f_i - g_i)^2 . \tag{23}$$

Here the sum is over a sufficient number of measured frequencies, w_i is a weighting factor chosen (usually either 0 or $1/g_i^2$, so that F is a measure of fractional deviation) to reflect one's degree of confidence in the measured frequency g_i (a function of signal strength and resonance width) and $f_i = \omega_i/2\pi$ is the ith calculated frequency. Note that the derivatives computed in eq. (20) are such that several resonant frequencies depend in almost exactly the same way on certain weighted sums of the c_{ij}. Thus many more than M resonances (where M is the number of parameters to be fit) must be measured for a meaningful fit to be achieved.

A systematic scheme is used to locate the minimum of F in the space of chosen parameters. This can be a 1-dimensional space if all we need to find is the compressibility of a fluid, or a 24-dimensional space if we need the 21 independent elastic constants of a triclinic crystal plus its three dimensions. The method we present here works in both these cases as well as many intermediate ones. In the process of searching for a viable minimization recipe we have tried several and settled on the Levenberg–Marquardt scheme [18] because it is relatively flexible, controllable, stable and reliable.

First we expand F in a Taylor series

$$F(\boldsymbol{x}) = F(\boldsymbol{x}_0) + (\boldsymbol{x} - \boldsymbol{x}_0)_\alpha F_{,\alpha}(\boldsymbol{x}_0) + \tfrac{1}{2}(\boldsymbol{x} - \boldsymbol{x}_0)_\alpha F_{,\alpha\beta}(\boldsymbol{x}_0)(\boldsymbol{x} - \boldsymbol{x}_0)_\beta + \cdots . \tag{24}$$

$\boldsymbol{x}$ is the vector whose components $\{\boldsymbol{x}_a\}$, $\alpha = 1, \ldots, M$, are the parameters we need to estimate (elastic constants, dimensions and Euler angles relating crystallographic axes to sample surfaces in a misaligned sample have all been successfully determined). This expansion is valid only in a limited domain such that $\boldsymbol{x} - \boldsymbol{x}_0$ is in some sense small, thus it is important to use any available information to guess accurately $\boldsymbol{x}_0$ at the start.

If F is a minimum at $\boldsymbol{x}$, then

$$F_{,\alpha}(\boldsymbol{x}) = 0 , \quad \alpha = 1, \ldots, M . \tag{25}$$

Using, eq. (24),

$$F_{,\alpha}(\boldsymbol{x}_0) + F_{,\alpha\beta}(\boldsymbol{x}_0)(\boldsymbol{x} - \boldsymbol{x}_0)_\beta = 0 \tag{26}$$

which, when solved iteratively for $\boldsymbol{x}$, is just Newton's method in M dimensions. The derivatives are

$$F_{,\alpha} = 2w_i(f_i - g_i)f_{i,\alpha} , \tag{27}$$

$$F_{,\alpha\beta} = 2w_i f_{i,\alpha} f_{i,\beta} + 2w_i(f_i - g_i)f_{i,\alpha\beta} . \tag{28}$$

The first derivatives $f_{i,\alpha}$ are given by eq. (20); we drop the second-derivative term $f_{i,\alpha\beta}$. One may make four arguments to justify this. First, the second term in eq. (28) is a sum over the measured frequencies; this sum will probably include about as many positive terms as negative ones, and consequently should be small. Secondly, dropping the second term will never affect the position of the minimum, only the route and speed of getting to it. Third, although $f_{i,\alpha\beta}$ can be expressed in terms of already computed eigenvectors and eigenvalues, actually evaluating it requires considerably more computer time than the evaluation of $f_{i,\alpha}$. Finally, to implement the minimization scheme one must obviously solve eq. (26) for $\boldsymbol{x}$, which may involve finding the inverse of $F_{,\alpha\beta}$, often a difficult thing to do if $F_{,\alpha\beta}$ is not positive definite (the first term in eq. (28) is positive-definite, but not the second). Following ref. [18], let

$$B_\alpha = w_i(f_i - g_i)f_{i,\alpha} , \tag{29}$$

$$A_{\alpha\beta} = w_i f_{i,\alpha} f_{i,\beta} , \tag{30}$$

and the solution of eq. (26) is

$$x_\alpha = x_{0\alpha} - A^{-1}_{\alpha\beta} B_\beta . \tag{31}$$

This equation is valid whenever eq. (24) is a good approximation, i.e. when x_α is close to the minimum. If not, a best guess is to move in a direction opposite to the gradient (downhill), i.e.

$$x_\alpha = x_{0\alpha} - \text{constant} * B_\alpha , \tag{32}$$

where the positive constant has dimensions x^2/F. $A_{\alpha\alpha}$ (no summation) has dimensions F/x^2 and is a measure of the $\alpha\alpha$th element of the F-surface curvature tensor. It therefore may be reasonably used to limit the distance moved in the αth direction in parameter space (this is important because there are many shallow local minima available to trap the solution. Such minima appear if a mode is too weak to be detected and no allowance is made for a missing mode in the group of measured frequencies, or if large steps are taken in following the gradient 'downhill'). Following Marquardt, introduce a dimensionless positive quantity Ω and replace eq. (31) with

$$x_\alpha = x_{0\alpha} - G_{\alpha\beta} B_\beta \tag{33}$$

where

$$G^{-1}_{\alpha\beta} = A_{\alpha\beta}(1 + \Omega\delta_{\alpha\beta}) . \tag{34}$$

without a sum in eq. (34). Equation (33) is identical to eq. (31) if $\Omega = 0$ and is very much like (32) for large Ω, when $\boldsymbol{G}$ becomes nearly diagonal. By choosing a large Ω we can proceed as cautiously as we like along the M-dimensional surface F, only decreasing Ω to zero when in the neighborhood of the minimum.

If by iterating eq. (33) a number of times convergence is achieved at a point $x_{\min}$ in M-dimensional parameter space where the gradients $B_\alpha = 0$, $\alpha = 1, \ldots, M$, then F may be expanded about that point:

$$F(\boldsymbol{x}) = F(x_{\min}) + \delta x_\alpha A_{\alpha\beta}(\boldsymbol{x}_{\min})\, \delta x_\beta + \cdots \tag{35}$$

where $\delta\boldsymbol{x} = \boldsymbol{x} - \boldsymbol{x}_{\min}$.

Because the curvature of F in different directions varies over as much as two orders of magnitude at the minimum, the accuracy for determining $\boldsymbol{x}_{\min}$ is very different for different parameters. Recognizing that $2\boldsymbol{A}$ is just the inverse of the covariance matrix for this problem, diagonalizing it (or equivalently, $\boldsymbol{G}$) yields M eigenvectors $\boldsymbol{y}^\mu$ and eigenvalues σ^2_μ. Specifically,

$$G_{\alpha\beta} y^\mu_\beta = 2\sigma^2_\mu y^\mu_\alpha . \tag{36}$$

In terms of these variances and eigenvectors eq. (35) becomes

$$F(\boldsymbol{x}) = F(\boldsymbol{x}_{\min}) + (\delta\boldsymbol{x}, \boldsymbol{y}^\mu)^2/2\sigma^2_\mu . \tag{37}$$

Here $(\delta\boldsymbol{x}, \boldsymbol{y}^\mu)$ is the inner product of two vectors, and because y^μ is a unit vector it is just the projection of $\delta\boldsymbol{x}$ in the $\boldsymbol{y}^\mu$ direction. So eq. (37)

tells us the shape of the surface F near the minimum. The surfaces of constant F are ellipsoids in M-dimensional parameter space with semi-major axes in the $\{y^\mu\}$ directions. The lengths of the semi-major axes are given by

$$s_\mu = \sigma_\mu (2\delta F)^{1/2} \tag{38}$$

where δF is the amount by which F exceeds the minimum. In practice it is often true that one or more of the σ_μ's is quite large, meaning that a large uncertainty is attached to the corresponding linear combination of the x_i's given by $(\delta x, y^\mu)$. Thus probable errors cannot be attached easily to individual elastic constants (and/or dimensions), but only to these linear combinations of them. We estimate the error for a particular parameter x_i by examining several of these linear combinations. In this way the sharpness of the minimum for a particular parameter and thus an error estimate for that parameter may be determined. The error estimate is very sensitive to sample geometry errors including chipped corners for a RP and inhomogeneities. Such errors may make the absolute minimum for F shallow and introduce other local minima that may trap the solution in the wrong place. The effect is compounded if a mode is missed. For a measurement with one or two missing modes and a 5 μm parallelism error in 2 mm it is essentially impossible to obtain an accurate (20% errors are easy to get) value in a cubic material for c_{11} or c_{12}; however c_{44} is always reasonably accurately obtained. Typically with a 'good' fit and where not more than two modes are missed out of 30, the RMS error between fitted and measured frequencies is less than 0.1%, the solution does not get trapped in a local minimum, and a change in this error of 2% is larger than all reproducibility and other error sources occurring in the measurement. Thus an M-dimensional ellipsoid in parameter space surrounding the minimum in F with a surface corresponding to a 2% increase in χ^2 provides a realistic error estimate for determination of parameters. Using this criterion, the compressional moduli (c_{ii}, $i = 1, 3$) are determined to better than 1%, shear moduli (c_{ii}, $i = 4, 6$) to 0.02% and off-diagonal moduli to better than 3%. This way of determining errors can be tested directly by making the dimensions of the sample free parameters. To circumvent the ambiguity mentioned above, we add to eq. (23) a term $\Delta(d_1 d_2 d_3 - V/8)^2$, which, for large Δ, has the effect of fixing the volume of the RP. Using measured values as the initial guess, for good data on a sample with good geometry, the fitted dimensions are typically within 2 μm (0.1%) of the measured value, the limit of our accuracy for length measurement.

2.2. Sample preparation

As described above, one can easily fit to a local and incorrect minimum in modulus space with very large concommitant errors in parameter determination if (1) the sample geometry and properties are not consistent with the mechanical model used for the computation, (2) some resonances are missed (i.e. f_i is paired with the wrong g_i in eq. (23)) or (3) the resonant frequencies are incorrectly measured. To achieved an accurate fit the faces of a millimeter-sized RP sample must be accurate to 2 μm or better. This is easily accomplished using ground steel shims and a glass plate as shown in fig. 1. The shims, surface-ground to be 10 to 50 μm thinner than the distance between sample faces to be polished, and with edges squared up in an ordinary milling machine, are arranged as shown on a flat glass plate coated with molten wax [19] and held down with a large magnet. The X-ray oriented sample is trapped by the shims and polished on 15 μm and then 3 μm optical lapping paper [20] using an appropriate lubricant such as kerosene. That the shims can force a sample face to be either parallel or perpendicular to the glass depending on how pressure is applied to the sample as the wax cools is crucial. In addition, as the sample nears completion, the shims support the sample edges, ensuring that sharp edges and corners are produced, especially for brittle materials such as La_2CuO_4. This appears to be important both for accuracy and to minimize the number of missed modes. There is no definite way that we know of for the quantifying requisite corner and edge sharpness.

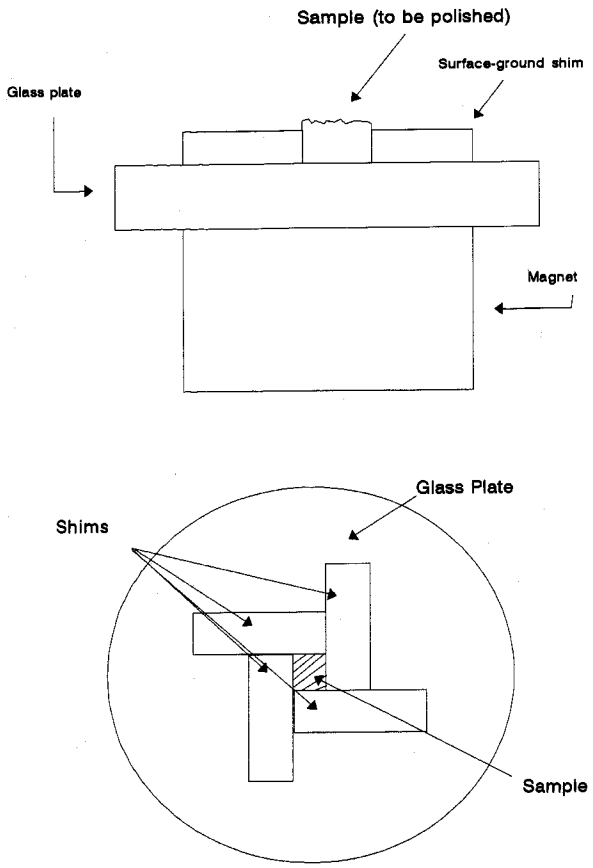

Fig. 1. Shown is the arrangement of ground steel shims on a glass plate used for obtaining an accurate rectangular parallelipiped from an as-grown oriented single crystal.

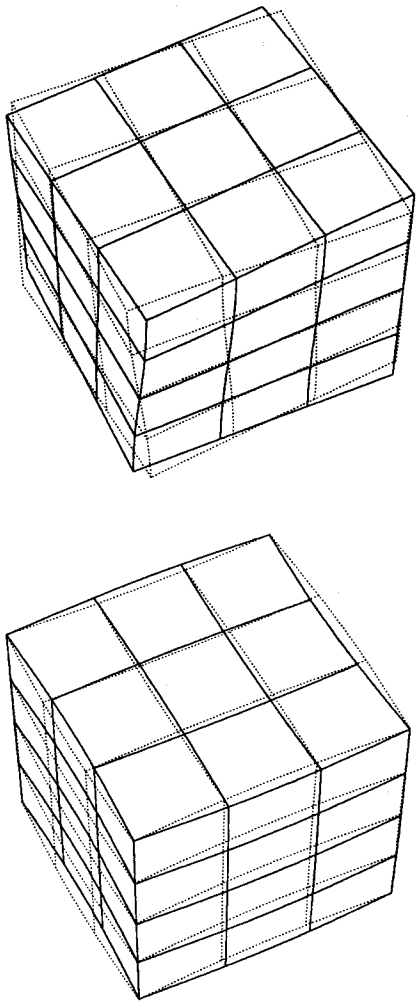

Fig. 2. Eigenvectors (local instantaneous peak displacements) for $k = 4$, a pure shear mode and $k = 5$, the only mode type for which the volume oscillates are displayed. The $k = 5$ mode illustrates how a node can occur near a corner, making it very difficult to observe that mode.

2.3. Hardware

Even with a well-prepared sample, certain modes, especially those having $k = 5$ (the only mode type where the volume oscillates) may have nodes near the corners of the sample. Computation of the mode shape is a simple addition to the codes used to find resonant frequencies, and the result for two mode types is shown in fig. 2. Because the task is to excite resonances, it is important to drive the sample at a low-symmetry location to excite as many modes as possible. The lowest symmetry point on a RP sample is the corner, thus this is the most desirable point to drive and detect, an important principle discovered by Demarest [11] and Anderson et al. [12], and derived, group-theoretically, by Mochizuki [21]. Moreover, the corners have a low mechanical impedance so that touching them with a transducer has minimal (less than a 10^{-5} fractional frequency shift) effect on the free-surface boundary conditions if the contact force is low (10^3 dynes or less). Other excitation schemes have also been used, such as electromagnetic [22] and polyvinylidene fluoride strips [23], with mixed sucess, in the sense that

the ultimate accuracy of determination of the free-sample resonances is not as good as for point contact.

Surprisingly, the lowest modes, even for an RP sample, are usually pure shear modes. Thus even if moduli and shape conspire to force a node to be near a corner, thereby making it so weak that it may be missed, the first several modes will generally determine the shear moduli to 1% or so, providing a good guess for them in the inversion calculation. The inversion code now has somewhat less work to do, making it harder to fall into a false minimum. More important, though, is that anything that helps ensure a good initial guess for the moduli should be used, including published values, because with a good starting point and the use of only the first five or ten resonances, the first pass of the code may help identify places where a mode is missing. Then a more careful scan or a remount of the sample may reveal the mode. There are other ways of finding missing modes using simple modifications to the apparatus described below [24], or by simply inserting, measuring and removing the sample several times. We cannot overstress the importance of finding nearly (95% or better) all modes before relying on the analysis of the data.

The hardware and electronics used to obtain accurate resonance data include a cryostat or furnace, transducers, a preamplifier, amplifier and mixer/filter or some equivalent. The electronic components and transducers used in our and Anderson's systems [25] are now commercially available from Quatro Corp. [26]. We will begin the hardware discussion with the transducers and work our way back to the PC-AT compatible computer used as a controller. Although other approaches will work, the one described here has been demonstrated to produce sufficiently high relative and absolute accuracy that overall errors are determined by temperature shifts and intrinsic sample preparation problems.

To measure resonances of the sample it is important to eliminate the resonant response of the apparatus, or extra modes may be observed. Because most samples in the size range of 1 mm have resonances above about 0.4 MHz, and 30 or more resonances below 3 MHz, the transducers used to excite and detect must be either damped or nonresonant in this frequency range. Damping does not work well over such a large range of frequencies or at 20 K, thus the nonresonant approach is best. However, all transducer materials have sound velocities comparable to the samples measured. One cannot get around this by using electrostatic, magnetic or optical detection schemes. The optical ones are much too noisy. Magnetic schemes, occasionally used by others [22], suffer from two serious problems. The first is that the sample must be either ferromagnetic or conducting or coated with a ferromagnetic or thick conducting layer. Even 1 μm of ferromagnetic layer can be a 0.2% perturbation on small samples, but worse still, the ferromagnet does not have a symmetric elastic tensor. Second, the coil used to drive or detect interacts mechanically with the sample via a magnetic field. Thus the usually numerous coil resonances shift and degrade the sample modes as well as perhaps introducing some new ones. This is known as 'coil disease' in NMR measurements [27]. Electrostatic systems have similar problems. The solution, applicable to direct contact (and electrostatic and magnetic drive systems as is obvious after a moment's reflection) is not to make very small, and therefore very weak transducers but to construct the transducer mostly out of single-crystal diamond. Our system [25] uses commercial 30 MHz compressional mode $LiNbO_3$ discs 1.5 mm in diameter and approximately 0.1 mm thick [28]. Such discs have a thickness mode of 30 MHz but bending modes near 180 kHz. However, using our cylinder code we know that a diamond cylinder 1.5 mm in diameter and 1.0 mm long has a lowest mode of 4.47 MHz. Thus if we bond the diamond to the transducer, the assembly has a lowest mode near 4 MHz. The diamond also acts as an inertial load, so that the response of the $LiNbO_3$ in direct contact with the sample is enhanced by the diamond behind it. We also use a Ag-coated polyimide film 25 μm thick with 1 μm of evaporated Ag as the ground plane, and a strip of this material 1.5 mm wide as a low inductance, low mechanical Q electrical contact by inserting the

strip between diamond and $LiNbO_3$. This strip also helps damp the 4 MHz and above assembly resonances. All joints are made with a nonconducting epoxy [29] because at these frequencies no direct electrical contact with the transducer is required, capacitive coupling is sufficient. The transducer assembly is shown in fig. 3.

In order to minimize transducer loading effects on the sample, we mount the transducers in a Mg machined 'tone arm' assembly, shown in fig. 4 schematically. This assembly provides of order 1 g of unbalanced mass above the transducer to provide a low contact force. The tone arm is suspended on 1 mm wide strips of Ag-coated polyimide film, the same used in the transducer. The width of the film provides a low-inductance electrical ground with excellent low-temperature

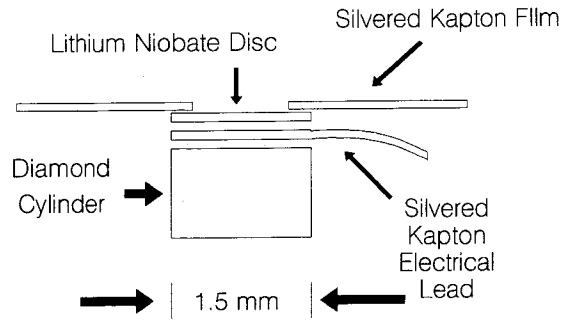

Fig. 3. Shown is a schematic of the diamond/polyimide/$LiNbO_3$ composite transducer used for all the measurements.

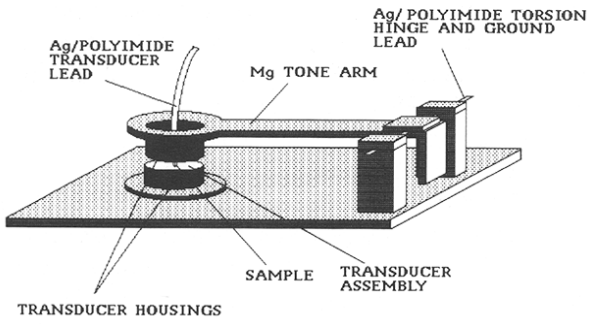

Fig. 4. The sketch here roughly illustrates how mechanical contact is made to the sample while preserving electrical shielding and maintaining a low contact force. This arrangement works well from 2 K, the lowest temperature we are set up to reach, up to the temperature at which the epoxy bonds in the transducers fail.

properties. The combination of low contact force and small, nonresonant transducers produces signals that are much weaker than those used by Ohno, Sumino and colleagues [15,30]. Their measurements were always made using a force balance that enabled resonant frequencies to be measured at successively lower contact forces. The frequencies shifted substantially (0.1%–0.5%) as force decreased, and the extrapolated asymptote was used as the zero-force frequency. With our system, even at comparable contact force, we observe less than 20 ppm frequency shifts for changes in loading from 2 g to 0.5 g. The shifts observed in refs. [15] and [30] appear to be primarily associated with high drive levels, and are absent for us. This is important because it greatly reduces both the amount of data required and the possibility of shifting the sample accidentally during a run, a problem that can cause artificial discontinuities in both frequencies and Q. Another effect appearing in Anderson's system is associated with alumina buffer rods [31]. These rods were necessary to isolate the transducers from temperatures exceeding an astonishing 2000 K, the highest temperatures ever used in a conventional ultrasound measurement system. Because the rods were long (i.e. several orders of magnitude longer than the largest sample dimension) they operated in the reverberation limit. That is, at the frequencies of interest for sample resonances, the rods themselves had such a higher mode density that the modes overlap strongly. As frequency is swept, the response of the buffer rods is convoluted with the sample response producing essentially random amplitude and phase mechanical motion, but with resonances still clearly detectable. The result is the observation of non-Lorentzian line shapes for the sample resonances, making it difficult to determine accurately either the center frequency or the Q. However, considering the temperatures reached, and with no obvious cure, Anderson was forced to use such an approach. For most other system designs, buffer rods should be avoided. A similar effect in our system is associated with the gas surrounding the sample which provides an undesirable ultrasound path between transducers in the reverberation limit. A disk of

ordinary filter paper with a small hole punched in the center, and split in half was constructed and inserted between transducer assemblies and surrounding the sample. This completely eliminates the gas path for ultrasound and thus minimizes gas resonances.

To access temperatures from 20 K to 400 K, our measurement cell is inserted into a vacuum-insulated cylinder. One end of the cylinder (or flow cryostat) is open, the other end is connected via vacuum insulated tubing (a conventional liquid-He transfer line) to the gas space above a liquid-He storage dewar. Inside the dewar, below the liquid level is a 1 kΩ, 2 W carbon resistor. This resistor is heated using an ordinary power-line-type variable autotransformer, with applied voltages up to about 30 VAC. The cold boil-off gas passes through the transfer line into the insulated cylinder and around the measurement cell. A second 50 Ω heater, constructed of 10 Ω/m cotton-insulated resistance wire (the wire is simply wadded up into a rough ball) is inserted in the gas flow path at the flow cryostat/transfer tube joint and is controlled using any commercial cryogenic temperature controller. Temperature sensing is via a silicon diode thermometer mounted inside the RUS cell within a few millimeters of the sample. This arrangement is shown schematically in fig. 5, and is capable of 20 mK temperature control.

The weak signals produced by our transducers and low contact force require the best possible signal/noise ratio (s/n) for the receiver electronics to ensure detection of as many modes as possible. The electronics design is centered around the electrical equivalent circuit for our transducer assembly over the frequencies of interest, essentially a pure 10 pF capacitor. Signals produced are in the tens of microvolt range and up. To detect such signals, two basic approaches can be taken. The one we reject is to use a broadband excitation pulse and Fourier transform the result. This is the best approach if large signals and overlapping modes are present [32]. However, to ensure that we do not miss even the weakest modes, and because the most usable samples have a mechanical Q in excess of 500, mode overlap is not a problem but s/n is. The broadband approach must have an electronic bandwidth exceeding that of the group of resonances to be measured, and must also signal average a measurement having a low duty cycle. That is, to average the signal (and noise over the receiver bandwidth) for some amount of measurement time, many excitation pulses must be generated, digitized time series taken, data

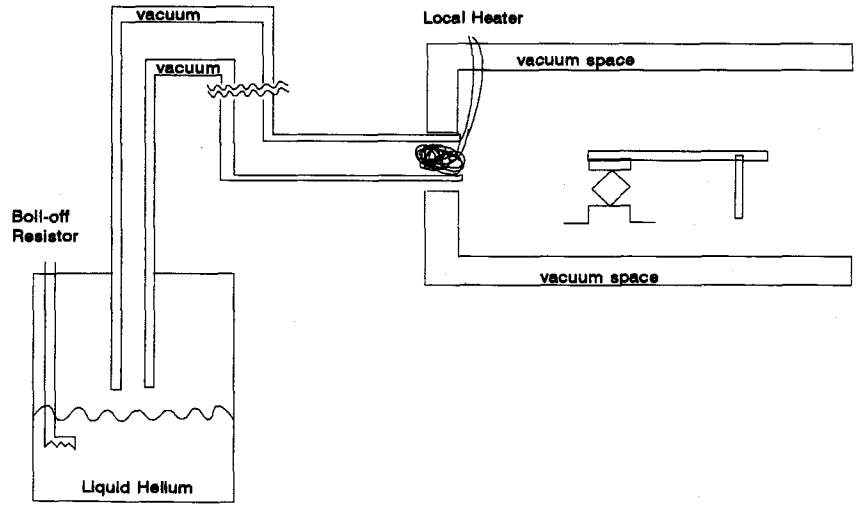

Fig. 5. Shown is the arrangement of the He storage dewar, transfer line and simple vacuum-insulated chamber that make up the flow cryostat that is so convenient for RUS.

transferred between pulses etc. Thus most of real time is spent with no signal present. Moreover, because measurements are made only in regions of frequency space where the sample exhibits mostly well-separated very sharp modes, any broadband system is acquiring much data that contains no information. Finally, for sharp, Lorentzian, well-separated modes, phase information is unnecessary. We have, therefore, chosen to use a swept sine approach based on a heterodyne receiver.

A heterodyne/swept-sine receiver (HSSR) can have an arbitrarily narrow bandwidth, has a duty cycle of unity, need only measure where resonances exist, and can signal average for arbitrarily long times a signal from which most of the noise is already eliminated using digital detection of the final, high-amplitude information-containing output of the analog section of the receiver. As with any receiver, the unavoidable noise is controlled primarily by the preamplification stage. The best approach for preamplification is to locate a JFET preamp very close to the receive transducer. In this way, the shunt effect of the capacitance (easily 100 pF) of cables connecting the 10 pF transducer to the preamp is eliminated. However, this would require a warm preamp to be located inside the flow cryostat, a complication we chose to forego. Instead, we use an accurately unity gain preamp at the end of a

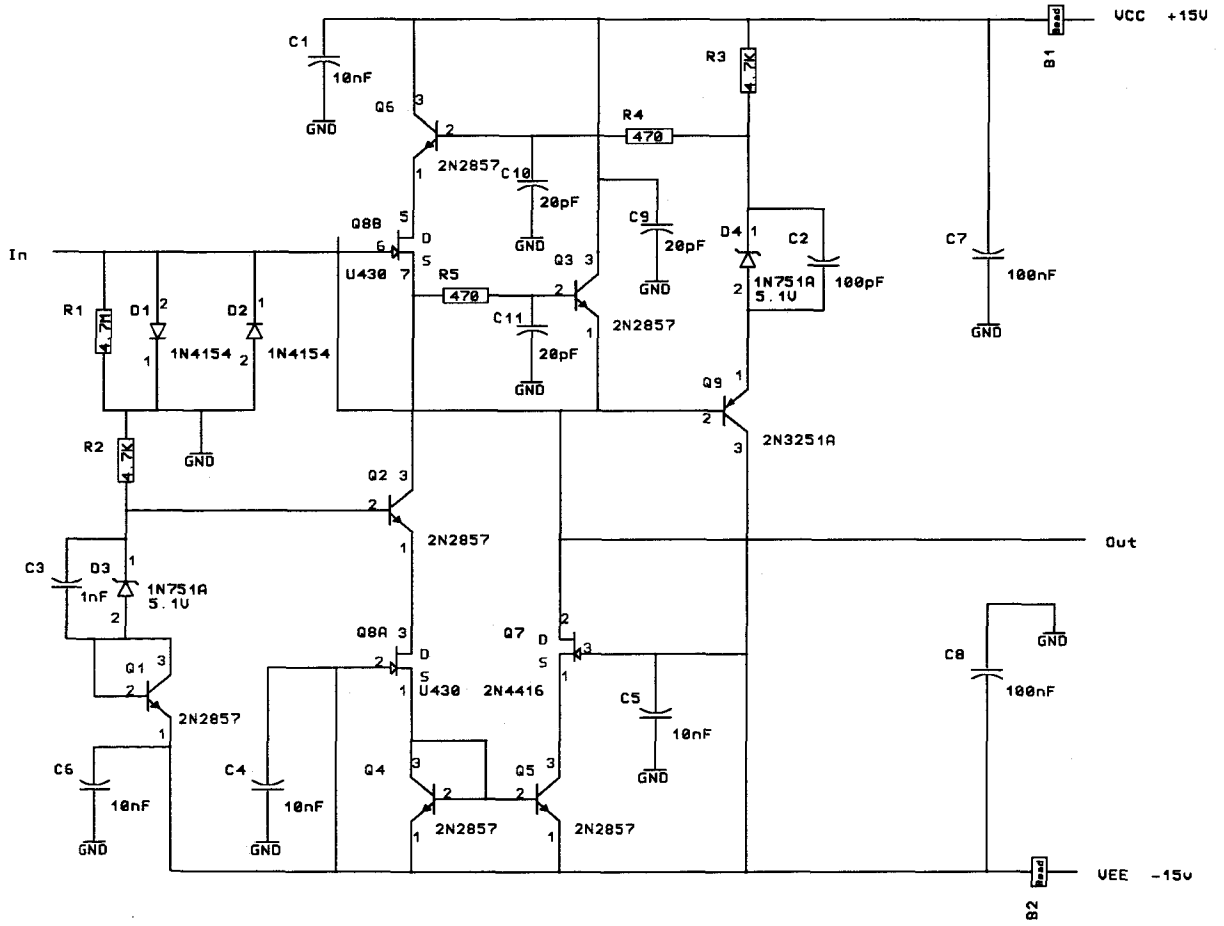

Fig. 6. We show here the schematic diagram of the low-noise unity-gain preamplifier used to bootstrap the cable capacitance of the transducer connection. The construction of this device requires very careful layout to prevent instabilities.

triaxial cable connecting preamp to transducer. By connecting the preamp output to the inner shield of the triax, we eliminate cable capacitance effects (this is known as a bootstrap or guard). This is only important because the preamp is voltage sensitive. For a current sensitive preamp or an op-amp type preamp, cable shunt capacitance has no effect on overall s/n. But for any type of preamp used with so much cable capacitance, much care must be taken to eliminate high-frequency phase shifts that could cause oscillation. This is why we have used low-inductance leads on the transducers and also why we find it easier to design a good JFET front end. The JFET unity-gain preamp shown schematically in fig. 6, modified from one described in Horowitz and Hill [33], is designed to have a bandwidth of 50 MHz, ensuring no unwanted phase shifts below 4 MHz, and has an input noise figure of a few $nV/Hz^{1/2}$, controlled primarily by the dual JFET. Because the triax effectively connects the output directly to the input, the design and layout of the circuitry is crucial. The inherent response of a HSSR is such that it is not the full bandwidth of the preamp, but instead the noise per unit bandwidth that is important for overall s/n.

The preamp is followed by a simple but quiet RF amplifier with a bandwidth of about 20 MHz based on an application note for the MAR-6 amplifier made by Mini-Circuits [34]. This stage, shown in fig. 7, has a voltage gain of 100.

Following the preamp is a mixer/filter shown in fig. 8 adapted from the data sheets from Motorola [35] and National Semiconductor [36]. This mixer performs an instantaneous multiplication of the RF transducer signal at frequency f, including whatever noise is present, with a (noise free) local oscillator (LO) signal at $f + \Delta f$, where Δf is the intermediate frequency or IF. The output of the mixer is, then, the amplifier noise upshifted in frequency by $f + \Delta f$, and information-containing signals at $2f + \Delta f$, and Δf. Because the noise is basically white, noise per unit bandwidth is unaffected. After the mixer is a state-variable analog filter tuned to Δf. Because the LO source is of constant amplitude, the amplitude of the mixer/filter IF output at Δf is

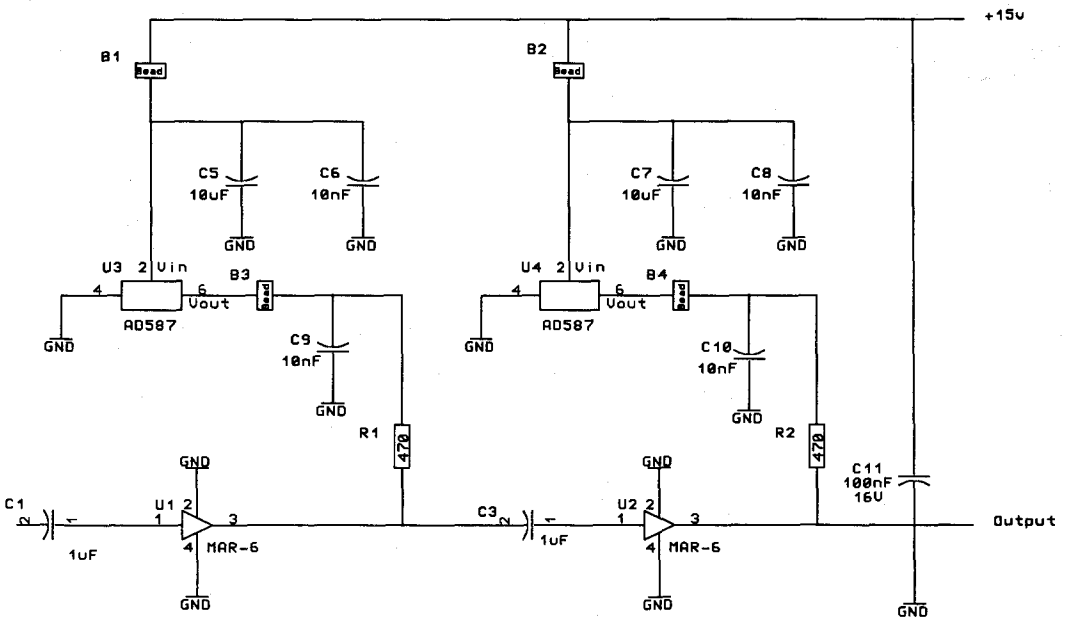

Fig. 7. Shown is the schematic diagram of the low-noise RF amplifier used for our RUS measurements, based on the MAR-6 integrated circuit. The layout of this circuit is extremely important.

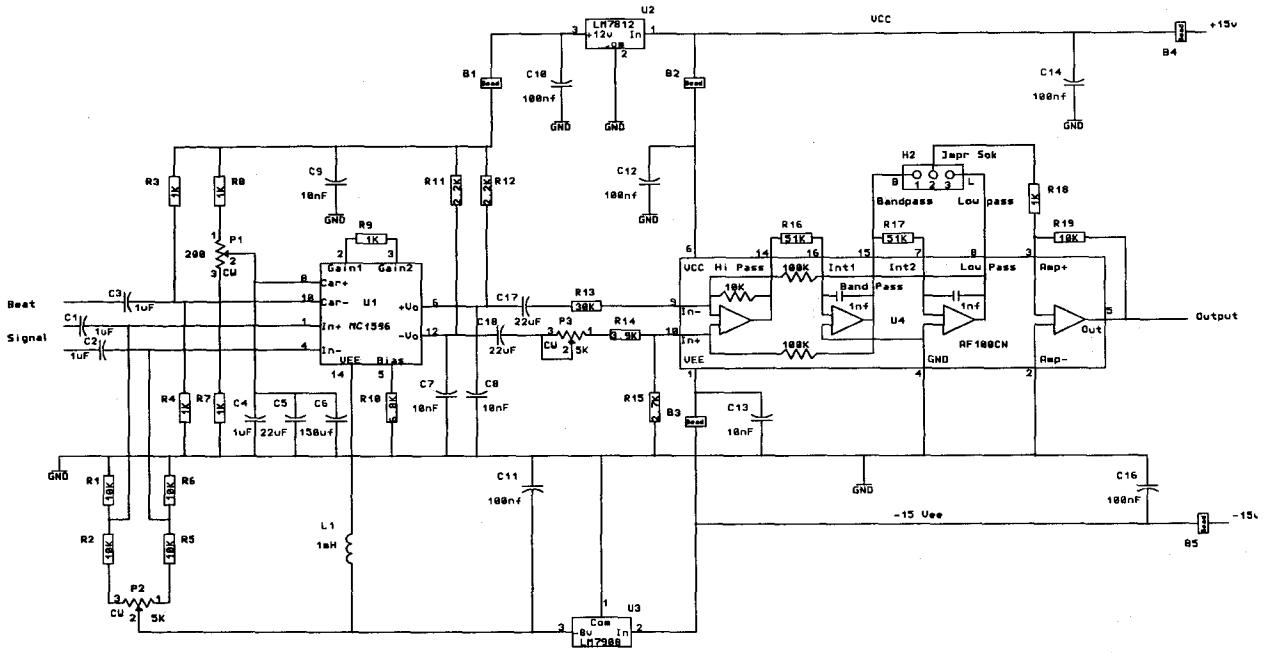

Fig. 8. The mixer/filter based on the widely used Motorola 1496 mixer IC and the National Semiconductor AF100 state-variable active filter is shown schematically. The layout of this circuit is extremely important.

proportional to the resonance signal at f. We use an IF frequency of 1 kHz and a filter bandwidth of 100 Hz. This yields a noise bandwidth 100 Hz wide at the filter output, but also limits the receiver response time to of order 10 ms. This is not a real limitation on the data acquisition rate because each sample resonance is stepped through using steps much narrower than the resonance width. Thus the receiver need only respond to incremental signal amplitude changes at sample resonance (i.e. if n steps are taken through one resonance then the receiver response time required is reduced by a factor of n).

At this point the resonance information wanted appears at a fixed IF frequency of 1 kHz combined with a 100 Hz wide slice of noise. To get the amplitude of the IF signal into a PC-AT type computer requires that it be 'detected'. The best approach is to use an analog to digital converter (ADC) to digitize the filter output such as an Analogic LSDAS-16, a 16-bit, 16 Channel, 50 kHz ADC [37]. By running the converter at 32 kHz and taking 320 readings, we acquire 10 cycles of the IF signal. We also acquire almost exactly 320 cycles of the most important interference source, the electric field associated with the VGA monitor of the computer. The *absolute value* of the 320 readings is averaged with software to generate the resonance amplitude at the frequency step chosen. The effect of this is (1) to produce a constant background offset arising from VGA interference, and (2) to signal average (equivalent to another 100 Hz bandpass filter) the IF signal over 10 cycles with no analog time constants to generate glitches if the measurement is started with uncontrolled phase of the IF signal (which it is).

A complete sweep through each individual mode is made using the above system and a dual digital synthesizer card to generate the LO and RF signals. The card we use was designed by us, is capable of 32 bit frequency and phase control and 15 bit amplitude control of two separate outputs, and is commercially available [26]. The card fits in a standard PC-AT slot, is controllable by Microsoft QuickBASIC or other languages and has a maximum output of 1 VAC (sufficient to drive the transducers directly) up to about

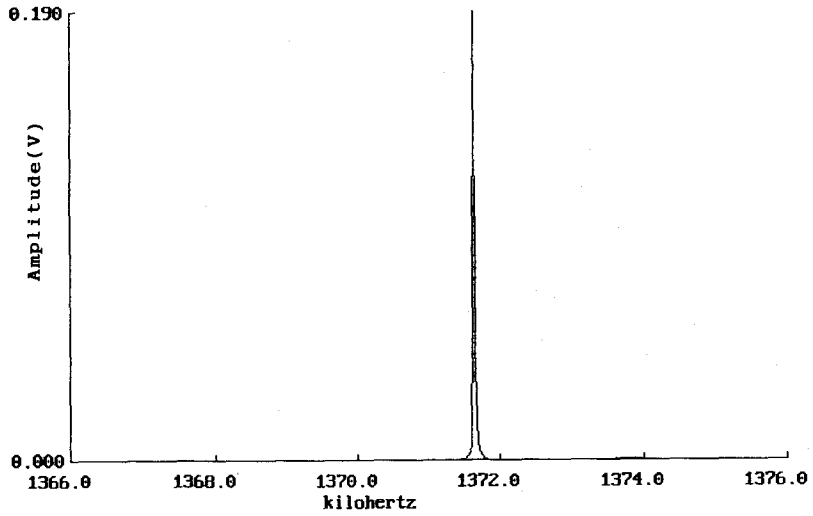

Fig. 9. A typical (and definitely not the best) resonance in the $La_{1.86}Sr_{0.14}CuO_4$ single crystal is shown to illustrate the quality of the data obtainable from a RUS measurement.

8 MHz. Other computer-controlled frequency synthesizers can be used successfully. A typical resonance is shown in fig. 9.

The resonance data acquired is processed to subtract background and then, using all the data acquired, a first moment of the usually Lorentzian resonances is computed. In this way, further noise reduction occurs so that we can determine reliably the center frequency of a resonance to about 3% or less of the linewidth. A complete experimental run would consist of (1) a search for all modes at room temperature, (2) acquisition of a data file produced by a narrow sweep through each resonance found, (3) a room-temperature fit to the moduli (and iteration of (1) and (2) if the fit is inadequate or predicts missing modes, and (4) a repeat of (2) for each temperature desired using sufficiently small temperature steps so as not to lose track of mode identifications.

3. Typical results

Having described the principles, procedures and hardware for making RUS measurements and analyzing the data, we present here some examples of the application of RUS to the study of structural phase transitions (SPT). The examples reviewed here are the soft-mode-driven SPTs in the perovskite system La_2CuO_4, which includes several high-temperature superconductors, and in $SrTiO_3$.

$SrTiO_3$ is a perovskite that undergoes a SPT from cubic (the high-temperature or 'symmetric' phase) to tetragonal (the low-temperature or 'unsymmetric' phase) crystal symmetry at 105 K. This material is particularly interesting because its SPT is a canonical example of a soft-mode [38] phase transition and has been well studied both theoretically [39] and experimentally using conventional ultrasonic techniques [40,41,42]. Furthermore, the perovskite structure and underlying titanium–oxygen octahedra in $SrTiO_3$ are very similar to the structure of the high-temperature superconductors La_2CuO_4 and $La_{2-x}Sr_xCuO_4$ to be discussed below. On a more practical level, large high-quality single crystals are readily available commercially, and no macroscopic fields develop at the SPT to complicate data analysis. We obtained a large single crystal [43] and prepared several RP samples (1.9 mm × 1.5 mm × 1.0 mm) as was described above.

The sample geometry was accurate to about 2 μm and the intrinsic quality was high so that

we were able to measure and fit the first 33 resonant frequencies at room temperature with an rms error of 0.075 percent. The values of the elastic moduli determined by the fit, as well as several sets of values from measurements by others, are shown in table 2. The agreement is excellent.

Our real interest in this material is not so much a test of RUS but rather a study of the details of the temperature dependence of the elastic moduli through the SPT. Because of the unique capability of RUS to determine all moduli simultaneously, precise comparisons between moduli can be made and compared to Ginsburg–Landau (G–L) type predictions. The SPT in $SrTiO_3$ occurs as a result of the softening of a particular zone edge lattice vibration, the tilting of the titanium–oxygen octahedra around the (1 0 0), (0 1 0) or (0 0 1) axes. As the frequency of this phonon decreases to zero, these octahedra develop a static displacement, reducing the crystal's symmetry to tetragonal and doubling the size of the unit cell. Because of the three-fold degeneracy of this octahedral tilt (rotation about x, y or z) the material also twins as it goes through the SPT, making RUS measurements difficult in the low-temperature phase.

Theoretically, this transition is well understood. The soft-mode description coupled with a G–L free energy enables accurate quantitative predictions to be made for the elastic response of the material through the transition. Rather than work with the complete expression for the free energy including all possible strains and the full three-component order parameter, discussed in detail elsewhere [39], we will focus here on a qualitative understanding by considering a single-strain and one-component order parameter. This is more than casually justified because if one knows which way the octahedra tilt, then use of a single-component order parameter causes no loss of generality. Because in an unstrained single crystal the order parameter does develop in a single direction, one certainly knows its direction after the fact. It is only important that one is careful with the group theory. That is, the full symmetry and number of required components of the order parameter are use to determine what terms must be included in a single-order-parameter description. Thus an accurate single-component-order-parameter free energy can be written

$$F = \tfrac{1}{2}c_0\varepsilon^2 + \tfrac{1}{2}\alpha(T - T_c)q^2 + \tfrac{1}{4}\beta q^4 + \tfrac{1}{2}\gamma\varepsilon q^2 \tag{39}$$

where ε is the strain, q the order parameter and α, β, γ and c_0 temperature-independent constants. The first term in eq. (39) represents the usual elastic energy, the second and third an expansion in the order parameter, and the last term the strain–order parameter coupling. Because the order parameter in this transition is a tilt in a mirror plane, only even powers appear (positive or negative tilts are equivalent energetically). Given such a free energy, the change in elastic moduli can be calculated by minimizing eq. (39) with respect to strain [44]. Such a minimization gives

$$c = c_0\,, \qquad T > T_c\,, \tag{40}$$

$$c = c_0 - \gamma^2/2\beta\,, \quad T < T_c\,. \tag{41}$$

Thus, a Ginsburg–Landau analysis of this phase transition predicts a step decrease in elastic moduli at the transition and, using the full crystal symmetry, predicts the relative size of the step for each individual modulus. Our data for the elastic moduli of $SrTiO_3$ as a function of temperature are shown in fig. 10. Each modulus increases with decreasing temperature from thermal contraction and then exhibits a sharp (but not step-like) decrease in the region near the transition, in agreement with the above analysis

Table 2
Room temperature elastic moduli (all values are in units of 10^{12} dyne/cm^2) of $SrTiO_3$ determined by RUS as well as by conventional ultrasonic techniques. The percentages after our data are the error estimates for the individual moduli, determined as discussed above.

c_{11}	c_{12}	c_{44}	Source
3.17	1.02	1.23	Ref. [40]
3.31	1.05	1.26	Ref. [41]
3.15 (0.2%)	1.02 (0.7%)	1.22 (0.01%)	This work

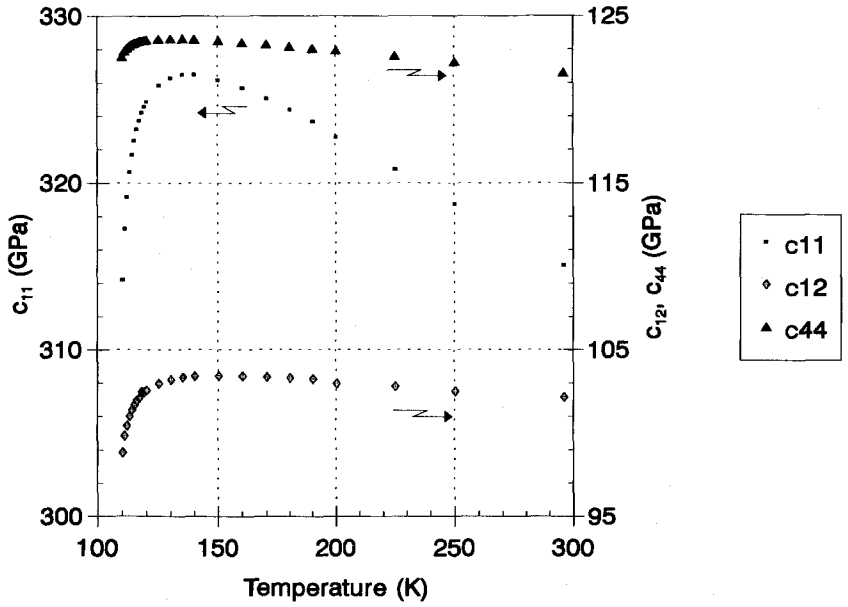

Fig. 10. The three elastic moduli of a single crystal of $SrTiO_3$ near the structural phase transition are shown as a function of temperature. These data were obtained using RUS.

as well as with the experimental work of others. Unfortunately, twinning of the crystal at the SPT prevents RUS from accessing the moduli in the unsymmetric phase so that some quantitative predictions of the Ginsburg–Landau theory cannot be tested by us. This has, however, been done by other groups using pulse-echo measurements and the results are in accord with theory [41]. Note that any ultrasound measurements in a twinned sample average over some set of moduli, and that to obtain useful information, some detailed knowledge of the twinning pattern and a model for backing out moduli are required. RUS is so sensitive to macroscopic twinning that usable data of any sort often cannot be obtained in a twinned sample because of substantial degradation of the resonance signals. This is typically not the case for pulse-echo, nor for RUS on microtwinned or polycrystal materials.

The departure from true step-like behavior can be attributed to both thermal fluctuations and to imperfections or defects in the crystal [45]. In order to verify this fact and to demonstrate the fundamental difference between this rounding and the effects observed in $La_{2-x}Sr_xCuO_4$, discussed below, we vacuum-annealed a RP of $SrTiO_3$ to create oxygen vacancies in an attempt to braden the transition. While a sharp decrease remains after annealing, the decrease is distinctly broader in the annealed sample, in agreement with previous work [42]. Having demonstrated that there are no surprises in a RUS study of $SrTiO_3$, we describe similar measurements on a more difficult system with results that prove to be not so accommodating.

Unlike $SrTiO_3$, La_2CuO_4 and also its high-temperature superconducting relative $La_{2-x}Sr_xCuO_4$ are not readily available as untwinned, morphologically perfect single crystals. The only such samples extant are in the 1 mm size range and require very considerable effort to produce. Thus conventional ultrasound techniques must be applied to either large, poor-quality twinned samples or not at all. In this system, the tetragonal to orthorhombic (TO) SPT occurs at 223 K for $x = 0.14$ and about 530 K for $x = 0.0$ [46]. In table 3 are the elastic moduli for an untwinned, orthorhombic crystal of La_2CuO_4 (1.735 mm × 1.536 mm × 1.108 mm, 7.026 g/cc) and also for a tetragonal crystal of $La_{1.86}Sr_{0.14}CuO_4$

Table 3
The full elastic moduli of $La_{1.6}Sr_{0.14}CuO_4$ and La_2CuO_4 in units of 10^{12} dyne/cm^2 determined using RUS. The first entry for $La_{1.86}Sr_{0.14}CuO_4$ is for the usual tetragonal basis. The second entry is simply the first one rotated by 45° such that a direct comparison to the orthorhombic stoichiometric compound can be made. The errors are about 1.3% for c_{ii}, $i = 1, 3$, 0.05% for c_{ii}, $i = 4$, 6, and 3.1% for the off-diagonal moduli for La_2CuO_4. The corresponding error estimates for $La_{1.86}Sr_{0.14}CuO_4$ are 0.25%, 0.01% and 1.0% respectively.

	c_{11}	c_{22}	c_{33}	c_{23}	c_{13}	c_{12}	c_{44}	c_{55}	c_{66}
$La_{1.86}Sr_{0.14}CuO_4$	2.666	–	2.571	–	0.992	0.649	0.677	–	0.587
$La_{1.86}Sr_{0.14}CuO_4$	2.245	–	2.571	–	0.992	1.071	0.677	–	1.009
La_2CuO_4	1.747	1.730	2.662	0.991	0.928	0.900	0.653	0.669	0.992

(2.470 mm × 2.267 mm × 2.192 mm, 6.946 g/cc) determined using RUS. The La_2CuO_4 crystal was grown by Canfield, Fisk and Kodali from a flux [47]. The Sr doped crystal was produced by Tanaka and Kojima using a travelling solvent/floating zone system [48]. We note that the axes of the La_2CuO_4 sample were not aligned with the crystallographic axes. Thus the fitting procedure had to determine not only the moduli and dimensions but also the crystal orientation. This takes far more computer time because the matrices to be inverted are no longer block diagonal. Nevertheless, the errors for the determination of moduli and angles are low because over 35 resonances were used in the fit.

We review here the microscopic deformations at the SPT in the La_2CuO_4 compounds, the Ginsburg–Landau Hamiltonian, and the expected effects on the sound velocities. Using RUS measurements on $La_{2-x}Sr_xCuO_4$ and a comparison with $SrTiO_3$, we present direct evidence for breakdown of tetragonal symmetry at the Brillouin zone center, show how this can explain the very strong temperature dependence of c_{66} above the TO SPT, and discuss some implications.

To understand what drives the TO transition in La_2CuO_4, consider first (fig. 11) the four Cu–O bonds that lie in the Cu–O plane and also form part of the O octahedra. Through the TO transition, these Cu–O bond lengths remain fixed [49]. What does change is the angle between the two O–Cu–O diagonals of the octahedra. In the tetragonal phase, the diagonals are perpendicular. In the orthorhombic phase they scissor slightly, doubling the unit cell. This Jahn–

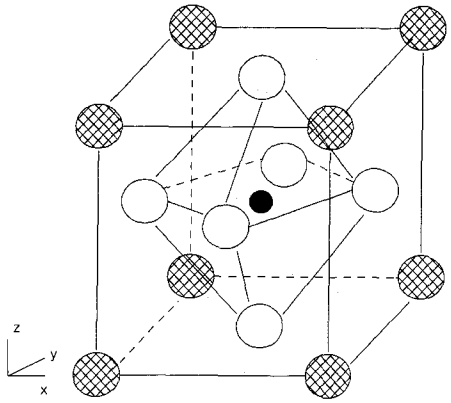

Fig. 11. We illustrate here the arrangement of ions (not to scale) of La_2CuO_4. Cu is the solid circle, the open circles are O and the shaded circles are La.

Teller-like distortion has the effect of increasing the length of either the (1 1 0) or the (1 $\underline{1}$ 0) axis. This is shown schematically in fig. 12. For the crystal to accomodate this, the Cu–O plane also buckles in the corresponding direction, taking the octahedra with it so that they tilt. This tilt is the x-point soft mode. Of course, a given octahedron could tilt in either of four possible directions, i.e. in the positive (1 1 0) direction, the negative (1 1 0) direction, the positive (1 $\underline{1}$ 0) direction, or the negative (1 $\underline{1}$ 0) direction. Thus both kinks (positive–negative tilt phase error) and twins (1 1 0) versus (1 $\underline{1}$ 0) tilt are possible, and the order parameter must have two components, q_1 and q_2.

Because any possible tilt preserves mirror symmetry, either sign of tilt is equivalent. Therefore any coupling of the Brillouin-zone-edge octahedron-tilt phonon mode to any zone-center

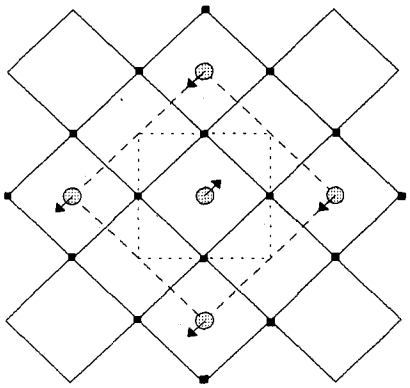

Fig. 12. Shown is a diagram showing the O atoms in the Cu–O plane (solid circles) and the O atoms at the apices of the O octahedra (shaded circles) projected onto the Cu–O plane. The Cu atoms are directly beneath the undisplaced O atoms and are not shown. Upon transition to the orthorhombic state, the apical O atoms displace as shown by the arrows (a twin would have displacements in the Cu–O plane perpendicular to those shown, i.e. turn the figure on its side). The tetragonal unit cell is the smaller dashed square, the orthorhombic one is the larger dashed square, although it is really a rectangle with the longer sides parallel to the arrows.

acoustic phonons must be quadratic in lowest order. Moreover, most of the effects of the phase transition are seen in c_{66}, the shear modulus for deformations of the Cu–O plane. This is also easily seen because when the O–Cu–O diagonals scissor, the square base of the tetragonal unit cell becomes a rhombus in the orthorhombic phase (fig. 12). Deforming the square into a rhombus is exactly equivalent to a c_{66} shear. We have, as yet, no measurements above the TO transition in La_2CuO_4 because our RUS cell cannot handle such temperatures. However, in $La_{1.86}Sr_{0.14}CuO_4$ the TO transition occurs at 223 K, a very convenient temperature.

In fig. 13 we show the resonant frequency of an eigenmode of the single crystal of $La_{1.86}Sr_{0.14}CuO_4$ as a function of temperature T and in fig. 14 we show $1/Q$ vs T where Q is the quality factor for the resonance. Numerical analysis of the motion establishes that the eigenmode of fig. 13 depends almost purely on c_{66}. Absent dynamical effects, we would treat the tempeature dependence of c_{66} with the same Ginsburg–Landau (G–L) Hamiltonian used for $SrTiO_3$. As with $SrTiO_3$, simple quadratic coupling and no dynamics produces only a step discontinuity in c_{66} at the SPT. This is not what the data show. The data fit a Curie–Weiss (C–W) softening of the form

$$c_{66}(T) = c_{66}(1 - T_0/(T - T_c)) \tag{42}$$

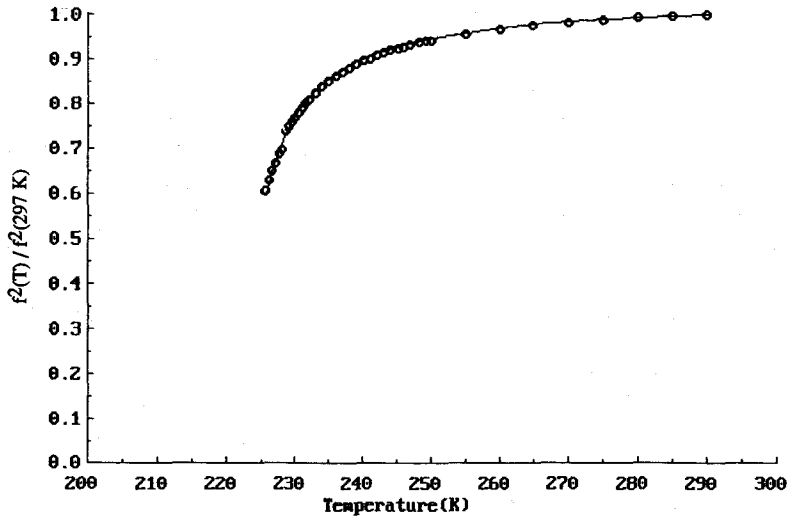

Fig. 13. Shown is the normalized resonant frequency squared (proportional to a modulus) for a $La_{1.86}Sr_{0.14}CuO_4$ mode that is nearly pure c_{66} as a function of temperature (circles). The solid line is a Curie–Weiss fit to the data. The gap in the data just below 230 K is evidence of symmetry-breaking effects.

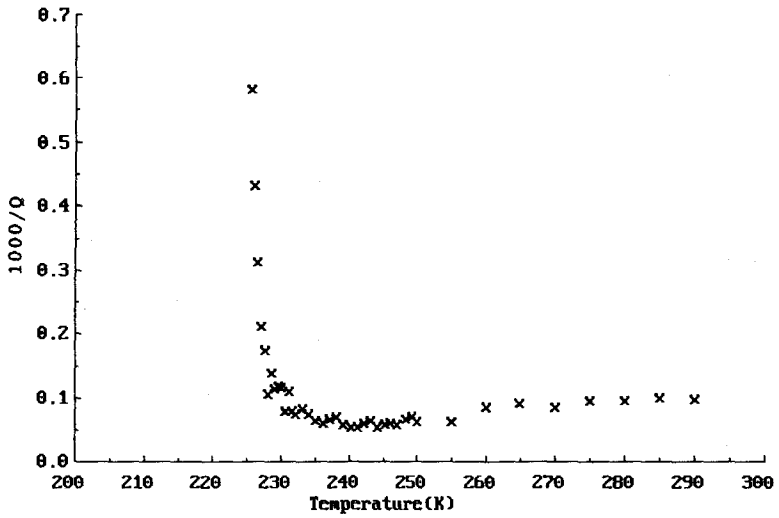

Fig. 14. The scaled inverse quality factor $1000/Q$ is proportional to the loss or ultrasonic attenuation in the single crystal of $La_{1.86}Sr_{0.14}CuO_4$. Very near the SPT at 223 K, the attenuation increases dramatically, but at temperatures well above the SPT but still in the Curie–Weiss region, no excess attenuation is observed.

where T_c is 223 K, c_{66} is a temperature-independent constant and the fit, shown as the solid line in fig. 13, is accurate to 0.2% over more than a decade in $T_0/(T - T_c)$.

Gaussian fluctuations of the order parameter [9], self-consistent phonons [7] and linear coupling between strain and order parameter [44] all yield a C–W behavior for c_{66}. For Gaussian fluctuations, the critical exponent for the specific heat and for the elastic moduli is $\Lambda = 2 - d/2$ where d is the dimension of the order parameter. In our system, the order parameter is two-dimensional, thus the critical exponent (the exponent of $1/(T - T_c)$) is unity, in agreement with the data. However, our C–W fit is over a temperature range of about 80 K ($T_0 = 1.47$ K). This is a very large range for fluctuations to be important, much larger than the range for the similar SPT in $SrTiO_3$. An upper-bound estimate for the fluctuations regime [9] is found by using a few lattice spacings for the coherence length, and by using a 1% ($SrTiO_3$ has about a 10% modulus discontinuity at its phase transition temperature) modulus discontinuity to obtain a fluctuation range of about 1 K, comparable to the region in fig. 14 where the ultrasonic attenuation increases sharply. Thus it appears very unlikely that 2-D Gaussian fluctuations can explain what we observe.

A self-consistent phonon treatment of the anharmonic potential associated with the zone-edge soft mode of the O octahedra can also produce C–W modulus softening [7]. For this sort of treatment to work, the zone-edge soft mode must be linearly coupled to the zone-center acoustic mode. The 1-D treatment in ref. [7] deals with this by inserting the anharmonic spring, used in the shell-model construct to develop the self-consistent phonon dispersion curve, in series with the ion cores. Thus this spring contributes to the potential energy for any value of k, the phonon wave vector.

Neutron scattering measurements [4] show that the soft mode is part of the phonon branch corresponding to c_{44}, not c_{66}. Without some linear coupling term to the c_{66} dispersion curve, it is not easy to see the applicability of self-consistent phonons. Were such a term to be added, the model would be forced to become explicitly 3-D, and because both the coupling and the energies would depend on the anharmonicity, the C–W exponent would likely be lost.

The third possibility we consider here is the

replacement of quadratic coupling with linear coupling (for $T > T_c$, the inclusion of the quadratic term has no effect with or without the linear term present) between order parameter and strain in eq. (39). Using the same justification for a single-component order parameter as in $SrTiO_3$ we find

$$F = \tfrac{1}{2}c_0\varepsilon^2 + \tfrac{1}{2}\alpha(T - T_c)q^2 + \tfrac{1}{4}\beta q^4 + \gamma\varepsilon q \qquad (43)$$

and

$$c_{66}(T) = c_{66} - \gamma^2/(T - T_c) \qquad \text{for } T > T_c\,, \qquad (44)$$

$$c_{66}(T) = c_{66} - \gamma^2/(2(T - T_c)) \qquad \text{for } T < T_c\,, \qquad (45)$$

as required to fit the data of fig. 13. To justify a linear coupling term, the $La_{1.86}Sr_{0.14}CuO_4$ crystal must be either nonlinear or nontetragonal.

In fig. 15 we plot the lowest eigenfrequencies of the $La_{1.86}Sr_{0.14}CuO_4$ crystal vs T and in fig. 16 are plotted the lowest two eigenmodes on an expanded scale, showing an avoided crossing of 2%. Note that in fig. 15 avoided crossings are observable in several places. The mechanical Lagrangian for analysis of the resonances of this material is based on a linear tetragonal solid [13,14]. The model produces eight orthogonal symmetry classes for the modes, therefore none of the avoided crossings should occur. Their existence can be explained only if the crystal is nonlinear, not tetragonal, or has excessive preparation errors.

This sample has a TO transition width of much less than 1 K as determined by the RUS variation of both Q and c_{66}, it has a superconducting T_c of 38 K, its faces have been ground parallel to better than 1 micron, some resonances have $Q > 70\,000$, it has near theoretical bulk density and no visible defects. There are, therefore, no sample preparation errors even remotely close to the few percent required to produce the observed avoided crossings. To test for anharmonicity, the measurements of fig. 16 were repeated at resonance amplitudes varying over an order of magnitude. All the scans were identical to about 0.01%, the limit of our temperature control precision. Thus no anharmonic affects are present.

X-ray [46] and elastic neutron scattering [4,49] studies of this material all indicate unambiguously that the structure is tetragonal. However, both types of probe operate at an effective $k = 0$. That

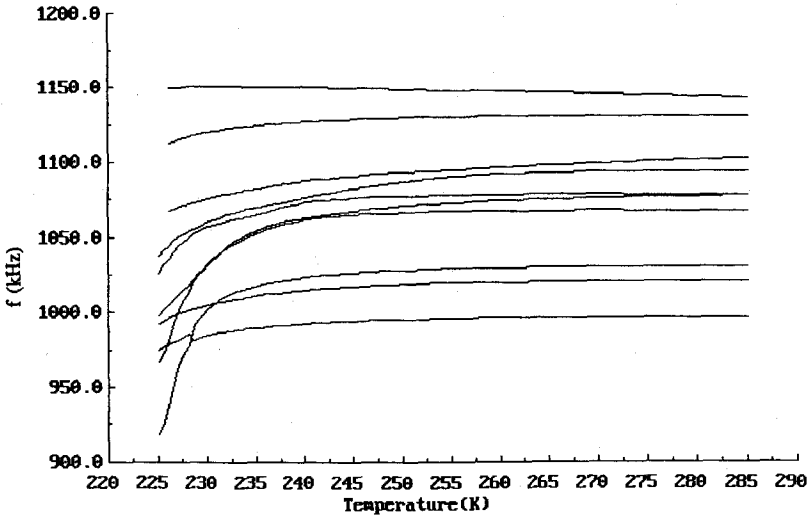

Fig. 15. This is a plot of many of the resonances of the $La_{1.86}Sr_{0.14}CuO_4$ single crystal as a function of temperature above the SPT. Avoided crossings are numerous.

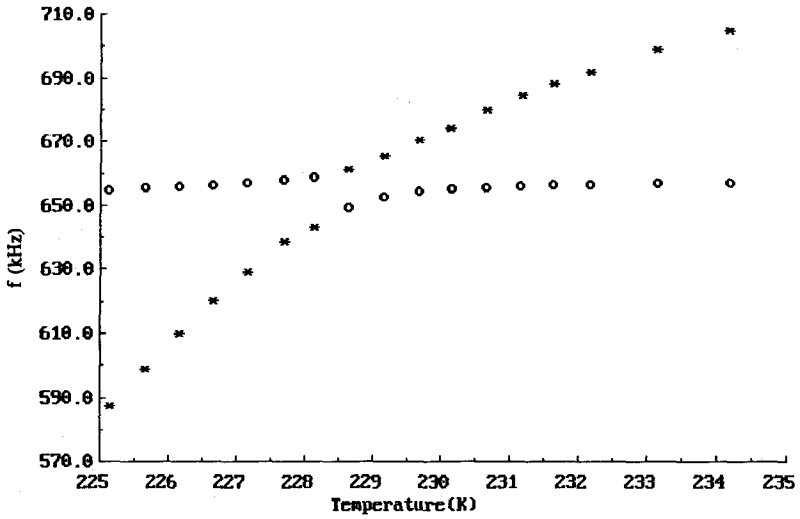

Fig. 16. Plotted are the data of fig. 13 for the c_{66} mode and also data for the c_{44} mode for the $La_{1.86}Sr_{0.14}CuO_4$ single crystal as a function of temperature. These modes have different symmetries so that no avoided crossing is expected. The surprisingly large effect may arise from symmetry-breaking at the Brillouin-zone-edge produced by Sr disorder combined with the soft-mode-driven SPT.

is, they average over many unit cells. Because RUS is also a $k = 0$ probe, it too should see a tetragonal structure. That it does not might be related to the destruction of zone-edge symmetry because of the disordered Sr doping. At small k, the Sr concentration fluctuations average out, and a tetragonal structure is observed. However, RUS is sensitive to the strain susceptibility. At temperatures well above (150 K or more) the TO transition, the x-point soft mode has negligible effect on c_{66} (see fig. 13). At temperatures somewhat above 300 K, all the sound velocities begin to decrease on cooling as a result of the coupling between the soft mode and the strains. This coupling might also carry with it a symmetry-breaking term at temperatures near the TO transition related to the total softening of c_{66}.

Such a symmetry-breaking effect is only observable if some effect, the SPT for this example, makes the moduli vary sufficiently rapidly that nominally orthogonal modes cross, and if the experimental probe can clearly separate the responses of the modes that cross. We know of no other ultrasound probe with this property. Thus RUS is capable of extracting new information as well as providing an alternative high-precision general ultrasound probe.

Acknowledgements

The authors wish to acknowledge Orson L. Anderson for many wonderful discussions, W. Gilbert Clark for his insights into electronics and instrumentation, Joe D. Thompson, Paul C. Canfield, Stuart E. Brown, Raymond M. Dixon and Selmer Wong for assistance with sample preparation and characterization, Philip B. Allen, Stuart A. Trugman and Lu J. Sham for tremendous patience and attention with the theoretical analyses and Tom Stockebrand for preparation of the printed circuits that make the electronics work so well. This work was performed under the auspices of the United States Department of Energy.

References

[1] B. Golding, W.H. Haemmerle, L.F. Schneemeyer and J.V. Waszczak, in: IEEE 1988 Ultrasonics Symposium (IEEE, Piscataway, 1988) p. 1079.

[2] T. Laegreid, Wu Ting, O.-M. Nes, M. Slaski, E. Eidem, E.J. Samuelsen, K. Fossheim and Y. Hidaka, in: Advances in Superconductivity II: Proceedings from the 2nd International Symposium on Superconductivity, November 14–17, 1989, Tsukaba, Ibaraki, Japan.

[3] P. Baumgart, S. Blumenroder, A. Erle, B. Hillebrands, G. Guntherodt and H. Schmidt, Solid State Commun. 69 (1989) 1135.
[4] P. Boni, J.D. Axe, G. Shirane, R.J. Birgeneau, D.R. Gabbe, H.P. Jenssen, M.A. Kastner, C.J. Peters, P.J. Picone and T.R. Thurston, Phys. Rev. B 38 (1988) 185.
[5] I.V. Aleksandrov, A.R. Goncharov and S.M. Stishov, JETP Lett. 47 (1988) 428.
[6] K. Kawasaki and A. Ikushima, Phys. Rev. B 1 (1970) 3143.
[7] A. Bussmann-Holder, A. Migliori, Z. Fisk, J.L. Sarrao, R.G. Leisure and S.-W. Cheong, Phys. Rev. Lett. 67 (1991) 512.
[8] L.D. Landau and E.M. Lifshitz, Statistical Physics, Part I (Pergamon Press, Oxford, 1980; 3rd ed.).
[9] S.K. Ma, Modern Theory of Critical Phenomena (Benjamin–Cummings, Reading, MA, 1976).
[10] R. Holland, J. Acoust. Soc. Am. 43 (1968) 988.
[11] H.H. Demarest, J. Acoust. Soc. Am. 49 (1971) 768.
[12] O.L. Anderson, E. Schreiber and N. Soga, Elastic Constants and Their Measurements (McGraw-Hill, New York, 1973).
[13] I. Ohno, J. Phys. Earth 24 (1976) 355.
[14] William M. Visscher, A. Migliori, T.M. Bell and R.A. Reinert, J. Acoust. Soc. Am. 90 (1991) 2154.
[15] I. Ohno, Phys. Chem. Minerals 17 (1990) 371.
[16] H. Oda, O.L. Anderson and Isao Suzuki, in: Proceedings of the 28th Annual Technical Meeting of the Society of Engineering Sciences, November 6–8, 1991, Gainesville, FL.
[17] B.T. Smith, J.M. Boyle, J.J. Dongarra, B.S. Garbow, Y. Ikebe, V.C. Klema and C.B. Moler, in: Matrix Eigensystem Routines – EISPACK Guide, Lecture Notes in Computer Science No. 6, eds. G. Goos and J. Hartmanis (Springer, New York, 1976); B.S. Garbow, J.M. Boyle, J.J. Dongarra and C.B. Moler, in: Matrix Eigensystem Routines – EISPACK Guide Extension, Lecture Notes in Computer Science No. 51, eds. G. Goos and J. Hartmanis (Springer, New York, 1977).
[18] W.H. Press, B.P. Lannery, S.A. Teukolsky and W.T. Vetterling, Numerical Recipes (Cambridge University Press, 1986).
[19] Crystal Bond; Aremco Products Inc., P.O. Box 429, Ossining, NY 10562.
[20] Optical Fiber Technologies, 2 Lyberty Way, Westford, MA 01886.
[21] E. Mochizuki, J. Phys. Earth 35 (1987) 159.
[22] W.L. Johnson, S.J. Norton, F. Benedec and R. Pless, J. Acoust. Soc. Am. 91 (1992) 2637.
[23] J.D. Maynard, J. Acoust. Soc. Am. 91 (1992) 1754.
[24] A. Stekel, J.L. Sarrao, T.M. Bell, Ming Lei, R.G. Leisure, William M. Visscher and A. Migliori, J. Acoust. Soc. Am. 92 (1992) 663.
[25] US patent # 4 976 148 Resonant Ultrasound Spectrometer, A. Migliori, William M. Visscher and Z. Fisk; US patent # 5 062 296 Resonant Ultrasound Spectroscopy, A. Migliori.
[26] Quatro Corp., 4300 San Mateo NE, Suite B-2890, Albuquerque, NM 87110.
[27] W.G. Clark, Rev. Sci. Instr. 35 (1964) 316.
[28] Valpey-Fisher, Ultrasound Division, 75-T South St., Hopkington, MA 01748.
[29] Any low-viscosity, clear epoxy, e.g. Stycast 1266; Emerson and Cuming Inc., 77 Dragon Ct., Woburn, MA 01888.
[30] Y. Sumino, I. Ohno, T. Goto and M. Kumazawa, J. Phys. Earth 24 (1976) 263.
[31] O. L. Anderson and T. Goto, Physics of the Earth and Planetary Interiors 55 (1989) 241.
[32] W.G. Clark, private communication.
[33] P. Horowitz and W. Hill, The Art of Electronics (Cambridge University Press, Cambridge, 1980; 1st ed.) p. 236.
[34] Mini-Circuits, P.O. Box 350166, Brooklyn, NY 11235–0003.
[35] MC1496 balanced Modulator–Demodulator, Motorola Semiconductor Products Inc., Box 20912, Phoenix, AZ 85036.
[36] AF100 Universal Active Filter, National Semiconductor Corp., 2900 Semiconductor Dr., P.O. Box 58090, Santa Clara, CA 95052–8090.
[37] Analogic Corp., 360 Audobon Rd., Wakefield, MA 01880.
[38] W. Cochran, Adv. Phys. 9 (1960) 387; P.W. Anderson, in: Fizika Dielektrov, ed. G.I. Sknavi (AN SSSR, Moscow, 1960) p. 290.
[39] J.C. Slonczewski and H. Thomas, Phys. Rev. B 1 (1970) 3599.
[40] R.O. Bell and G. Rupprecht, Phys. Rev. 129 (1963) 90.
[41] B. Luthi and T.J. Moran, Phys. Rev. B 2 (1970) 1211.
[42] D. Bauerle and W. Rehwald, Solid State Commun. 27 (1978) 1343.
[43] Sample supplied by I.D. Raistrick, Los Alamos National Laboratory.
[44] W. Rehwald, Adv. Phys. 22 (1973) 721.
[45] A.P. Levanyuk and A.S. Sigov, Defects and Structural Phase Transitions (Gordon and Breach, New York, 1989).
[46] R.M. Fleming, B. Batlogg, R.J. Cava and E.A. Rietman, Phys. Rev. B 35 (1987) 7191.
[47] S.-W. Cheong, J.D. Thompson and Z. Fisk, Physica C 158 (1989) 109.
[48] I. Tanaka and H. Kojima, Nature 337 (1989) 21.
[49] R.J. Cava, A. Santoro, D.W. Johnson Jr. and W.W. Rhodes, Phys. Rev. B 35 (1987) 6716.